Recycled steel fibre reinforced concrete failing in bending and in shear

Ziaaddin Zamanzadeh[a*], Lúcio Lourenço[b] and Joaquim Barros[c]

[a] *Civil engineering department, University of Minho, Guimarães, Portugal*

PhD Student, ISISE, Dep. Civil Engineering, University of Minho, Campus de Azurém, 4800-058 Guimarães, PORTUGAL, zia.zamanzadeh@gmail.com,  Tel: +351 915 106 760

* Corresponding author

[b] *CiviTest, Vila Nova de Famalicão, Portugal*

PhD Engineer, CiviTest, 4760-042 Vila Nova de Famalicão, PORTUGAL, luciolourenco@civitest.com, Tel: +351 918 786 805

[c] *Civil engineering department, University of Minho, Guimarães, Portugal*

Full Professor, ISISE, Dep. Civil Engineering, University of Minho, Campus de Azurém, 4800-058 Guimarães, PORTUGAL, barros@civil.uminho.pt, Tel: +351 253 510 210

## 1 Recycled steel fibre reinforced concrete failing in bending and in shear

2     Abstract: Recent research is showing that the addition of Recycled Steel Fibres
3     (RSF) from wasted tyres can decrease significantly the brittle behaviour of cement
4     based materials, by improving its toughness and post-cracking resistance. In this
5     sense, Recycled Steel Fibre Reinforced Concrete (RSFRC) seems to have the
6     potential to constitute a sustainable material for structural and non-structural
7     applications. To assess this potential, experimental and numerical research was
8     performed on the use of RSFRC in elements failing in bending and in beams failing
9     in shear. The values of the fracture mode I parameters of the developed RSFRC
10     were determined by performing inverse analysis with test results obtained in three
11     point notched beam bending tests. To assess the possibility of using RSF as shear
12     reinforcement in Reinforced Concrete (RC) beams, three point bending tests were
13     executed with three series of RSFRC beams flexurally reinforced with a relatively
14     high reinforcement ratio of longitudinal steel bars in order to assure shear failure
15     for all the tested beams. By performing material nonlinear simulations with a
16     computer program based on the finite element method (FEM), the applicability of
17     the fracture mode I crack constitutive law derived from the inverse analysis is
18     assessed for the prediction of the behaviour of these beams. The performance of
19     the formulation proposed by RILEM TC 162 TDF and CEB-FIP 2010 for the
20     prediction of the shear resistance of fibre reinforced concrete elements was also
21     evaluated.

22     Keywords: Recycled steel fibre reinforced concrete; fracture mode I parameters;
23     inverse analysis; shear reinforcement

## 1 Introduction

25 Over the past three decades, the potential of using Steel Fibre Reinforced Concrete

26 (SFRC) to improve the performance of statically determinate and indeterminate structures

27 has been investigated. The crack opening restraint provided by the reinforcement

28 mechanisms of steel fibres (herein designated as Industrial Steel Fibres, ISF) bridging the

29 crack surfaces (Cunha, 2010) lead to significant increase in terms of load carrying

30 capacity and energy absorption capability of concrete structures, mainly those of high

redundant support conditions, since stress redistribution provided by fibre reinforcement allows an ultimate load much higher than the cracking load (Lee et al., 2011; Barros et al., 2009; Voo & Foster, 2003). The available bibliography on the subject shows that steel fibre reinforcement can increase significantly the shear (Barros et al., 2014; Aoude et al., 2012; Susetyo et al., 2011) the flexural (Barros et al., 2014; Caggiano et al., 2012; De Montaignac et al., 2012; Barros & Figueiras, 1999) and the punching (Ventura-Gouveia et al., 2011; Safeer et al., 2004) resistance, as well as the durability (Kunieda et al., 2014; Lourenço et al., 2011; Banthia et al., 2010; Granju & Balouch, 2005) of concrete structures. On the other hand, recent research is showing that steel fibres originated from the industry of tyre recycling, herein designated as Recycled Steel Fibres (RSF), can also be a valuable reinforcement system to decrease significantly the brittle behaviour of cement based materials, by improving their toughness and post-cracking resistance. Recycled Steel Fibre Reinforced Concrete (RSFRC) is therefore becoming a promising candidate for both structural and non-structural applications (Aiello et al., 2009). The use of RSF as a reinforcement system of concrete elements has also beneficial environmental and economic impacts, since an added commercial value is given to a sub-product of the tyre recycling industry that, in general, is considered a waste product (Graeff et al., 2012; Neocleous et al., 2006). For a wider and reliable use of RSF in concrete construction important barriers, however, need to be overcome, such are those caused by the lack of knowledge with respect to: i) the technology of producing RSFRC with suitable properties for concrete construction industry; ii) the characterization of the relevant mechanical properties of RSFRC; iii) the design of RSFRC structures.

Reinforced concrete structural elements without adequate transverse reinforcement can fail abruptly in shear before reaching their full flexural capacity when exposed to a combination of flexural and shear forces (Hai, 2009). To prevent shear

1   failures, beams are traditionally reinforced with steel stirrups. Since shear failure is brittle

2   in nature, several design codes (ACI Committee 318, 2008; Eurocode, 2004; NZS4203,

3   1992) recommend a high percentage of steel stirrups in the critical regions (Cucchiara et

4   al., 2004). The application of steel stirrups in concrete elements, especially in those

5   composed of hollow sections, or composed of thin walled components, has significant

6   costs due to intense labour demands it requires. In structural concrete elements of

7   buildings in seismic risk zones, the density of steel stirrups and hoops may difficult to

8   obtain the desired concrete quality (Barros et al., 2014). Due to these reasons, the partial

9   or total substitution of steel fibres by steel stirrups has been studied by several researchers

10  (Centonze et al., 2012; Tlemat et al., 2004)

11       Experimental results evidenced that beams reinforced only with steel fibres

12  showed a similar (or even better) post-cracking behaviour than reference beams with the

13  minimum amount of steel stirrups recommended by Eurocode 2. Even when used in

14  beams reinforced with steel stirrups, steel fibres significantly improved the shear

15  resistance. Steel fibres also reduce the width of shear cracks, thus improving the concrete

16  durability and structural integrity (Meda et al., 2005).

17       The present study aims to contribute to increase the knowledge on the

18  characterization of the post cracking properties of RSFRC, on its use as shear

19  reinforcement, and on the design and advanced modelling of RSFRC beams failing in

20  shear. In this context an experimental program composed of tests with beams of concrete

21  reinforced with 45, 60 and 90 kg/m$^3$ of RSF was executed. The most recent methodologies

22  for the characterization of FRC were applied to the developed RSFRC. The potentialities

23  of RSFRC as a shear reinforcement of relatively shallow beams are also explored, and

24  the applicability of available design recommendations (RILEM TC 162-TDF, 2003;

25  CEB-FIP 2010, 2011) to predict the shear resistance of RSFRC beams is also assessed.

1  For the analysis of RSFRC beams failing in shear, material nonlinear simulations are

2  carried out using a computer program based on the finite element method (FEM). In these

3  analysis, the constitutive law that defines the fracture mode I of the developed RSFRC

4  was obtained by applying inverse analysis (Amin et al., 2013; Pereira et al., 2008; Tlemat

5  et al., 2006; Barros et al., 2005) to the results obtained in the three point notched beam

6  bending tests executed for the characterization of the post-cracking behaviour of RSFRC.

7  The applicability of this methodology is also discussed in the present work.

8  **2  Recycled Steel Fibre from waste tyres**

9  Tyre shredding and the cryogenic process can be used to mechanically extract RSF from

10  waste tyres. In addition, RSF can be obtained by utilizing anaerobic thermal degradation,

11  such as conventional pyrolysis and microwave-induced (AMAT, 2003). The RSF adopted

12  in the present experimental work was supplied by a Portuguese private company, and the

13  cryogenic process of waste tyres was the one adopted by this company. This process is

14  composed by the four following stages (see Figure 1): 1) whole tyre size is reduced by

15  various means; 2) tyres are then fed into cryo-chamber and frozen with liquid nitrogen to

16  -184 ºC; 3) hammer mill reduces crumb to particles of various sizes; 4) steel fibres are

17  removed magnetically. The RSF obtained from this process are characterized by different

18  diameters, lengths and shapes, and present irregular wrinkles (see Figure 2).

19  **3  Flexural behaviour of RSFRC**

20  *3.1  Test series and mix composition*

21  To assess the potentialities of RSF for the reinforcement of concrete elements, three series

22  of RSFRC specimens were subjected to three point notched beam bending tests.

23  Specimens reinforced with ISF were also considered for comparison purposes. Note that,

1    for all the specimens, mixes of similar concrete strength class (40 MPa, cylinders) were

2    used in order to perform a reliable comparison of the mechanical properties. The number

3    of specimens for each series and the content of steel fibres are indicated in Table 1. Since

4    a higher dispersion on the results was expected for the RSFRC, mainly for the two series

5    of smaller content of RSF, the number of specimens prepared for the corresponding

6    compositions was higher than for the concrete compositions reinforced with ISF.

7          To accommodate properly 45, 60 and 90 kg of RSF per cubic meter of concrete

8    with the aimed flowability and without segregation of the constituents, the organization

9    of the aggregate skeleton was optimized by considering the direct influence of the fibres

10    on the mix design methodology. In an attempt of assuring a suitable distribution of RSF,

11    during the execution of the concrete mixes, RSF were gradually added to the mixture. To

12    avoid the strong perturbation effect on the flowability of fresh concrete when RSF dosage

13    is increased, in the M_90 fly ash was used, and the content of cement, limestone filler

14    and fine river sand was increased. Table 2 shows the three mix proportions used (common

15    to RSFRC and Industrial Steel Fibres Reinforced Concrete, ISFRC).

16    *3.2   Test setup and methodology*

17    The specimen geometry (see Figure 3), the position and dimensions of the notch sawn

18    into the specimen, the loading and specimen support conditions, the characteristics for

19    both the equipment and measuring devices and the test procedures to characterize the

20    flexural behaviour of RSFRC are all given elsewhere (RILEM TC 162-TDF, 2003; CEB-

21    FIP 2010, 2011).

22          Figure 4 presents a typical relationship between the applied load and the Crack

23    Mouth Opening Displacement (*CMOD*) obtained from a three-point beam-bending test.

24    Using this type of relationship, the load at the limit of proportionality ($F_L$) and the

1 residual flexural tensile strength parameters ($f_{R,j}$) can be obtained. $F_L$ is the highest

2 value of the load recorded up to a deflection (or *CMOD*) of 0.05 mm.

3       Based on the force values for the $CMOD_j$ ($j = 1$ to 4, see Figure 4), the

4 corresponding force values ($F_j$) are obtained, and the derived residual flexural tensile

5 strength parameters are determined from the following equation:

$$f_{R,j} = \frac{3F_j L}{2bh_{sp}^2} \tag{1}$$

6 where: $b = 150$ mm and $L = 500$ mm are the width and the span of the specimen;

7 $h_{sp} = 125$ mm is the distance between the tip of the notch and the top of the cross section.

8 ### *3.3 Experimental results*

9 One of the main effects of the fibres is to control the crack propagation and maintain the

10 crack width in the limits according to structural concrete requirements. The fibre

11 reinforcement provides a residual strength in the post-cracking stage, which is much

12 higher than in the corresponding plain concrete (concrete of the same strength class but

13 without any reinforcement), resulting in a significant improvement of the material

14 toughness. The level of toughness depends on the efficiency of fibre reinforcement

15 mechanisms. Fibre pull-out should be the governing fibre failure mode in both RSFRC

16 and ISFRC.

17       In Figure 5a average curves of flexural stress vs CMOD are presented for RSFRC

18 specimens. It is verified that the increase of the fibre content has led to an increase of the

19 peak load and post cracking residual strength, as expected.

20       The flexural behaviour obtained in the three point bending tests with ISFRC

21 specimens is illustrated in Figure 5b. The comparison between the flexural behaviour of

RSFRC and ISFRC are depicted in Figure 6. The results of three point bending tests are analysed in term of equivalent and residual flexural tensile strength parameters and corresponding coefficient of variation (COV) for RSFRC (Table 3) and ISFRC (Table 4) specimens. From the data it can be observed that in the M45_RSF (45 kg of RSF per cubic meter of concrete) a larger dispersion of the results was obtained (a COV values higher than 18.5%), which can be justified by extra difficulties on assuring proper fibre distribution in the M45_RSF specimens. The graphical representation of the equivalent and residual flexural strength parameters for all the tested series is represented in Figure 7. From the obtained results it is verified that the deflection hardening phase registered in the ISFRC specimens (from crack initiation up to flexural tensile strength) was not developed in the RSFRC specimens. This indicates that fibre bridging mechanisms across the crack surfaces for relatively small crack width levels are not effective in the RSF due to the geometry and surface characteristics of these fibres. However, in the post-peak stage the RSFRC specimens have almost retained the maximum flexural tensile strength up to the ultimate crack width recorded in the executed tests (3.5 mm).

Figure 8 shows the relationship between $f_{eq,2}$ and $f_{eq,3}$ obtained in RSFRC specimens. A clear linear relationship emerges between these two parameters, which is in agreement with previous research on ISFRC specimens (Barros et al., 2005).

The relationships between $f_{eq,2}$ and $f_{R,1}$, and between $f_{eq,3}$ and $f_{R,4}$ are represented in Figure 9. Also a linear trend emerges between these parameters.

The characteristic values of the stress at the limit of proportionality vs fibre volume percentage ($V_f$) and the characteristic values of the residual flexural tensile strength parameters vs $V_f$ for all tested specimens in accordance with the recommendations of RILEM TC 162-TDF (2003) and CEB-FIP 2010 (2011) are reported in Figure 10.

For a wider comparison between RSFRC and SFRC, the database (DB) collected by Moraes Neto (2013) in terms of $f_{Ri}$ values was used in the present work. This DB includes $f_{Ri}$ values of ISFRC of hooked ends geometry configuration for the ISF, and presenting tensile strain softening, which is also the type of behaviour of both RSFRC and ISFRC considered in the present experimental program. Figure 11 compares $f_{R1} - f_{R3}$ and $f_{R1} - f_{R4}$ from the experimental results of DB with those obtained from RSFRC specimens. A similar trend emerges between the RSFRC and the DB results in terms of $f_{R1} - f_{R3}$ and $f_{R1} - f_{R4}$.

Figure 12 compares $f_{R,i}$ and $V_f$ from the experimental results of the DB with those obtained from the RSFRC specimens. It is verified that the increase of the fibre volume percentage in SFRC specimens (DB) leads to a higher increase of the residual flexural tensile strength parameters, comparatively with the values obtained for RSFRC specimens, which means that, for usual SFRC compositions, the fibre reinforcement effectiveness by increasing the fibre content is higher with ISF than with RSF. However, the development of mix design strategies for the RSFRC that assure proper fibre distribution up to fibre contents used in structural applications might attenuate this different fibre reinforcement effectiveness. In any case, the $f_{R,i}$ values obtained for the developed RSFRC are sufficiently high to create good perspectives for the use of these composites in certain applications.

## 4 Recycled steel fibres as a shear reinforcement of flexurally reinforced concrete beams

In this section the use of RSF (60 kg/m$^3$) as a shear reinforcement of RC beams is explored. The applicability of the design recommendations proposed by RILEM TC 162-TDF (2003) and CEB-FIP 2010 (2011) to estimate the contribution of

1  RSF for the shear resistance of RC beams is also assessed. For this purpose the average

2  values of the residual flexural tensile strength parameters of the RSFRC that were

3  obtained from the three point bending tests were used.


4  *4.1   Analytical formulations*

5  According to the CEB-FIP 2010 (2011), the shear capacity of the concrete elements, $V_{Rd}$,

6  comprises the shear capacity provided by SFRC, $V_{Rd,F}$, and by the steel stirrups $V_{Rd,s}$:

$$V_{Rd} = V_{Rd,F} + V_{Rd,s} \tag{2}$$

7  where

$$V_{Rd,F} = \left\{ \frac{0.18}{\gamma} \times K \left[ 100 \times \rho_1 \times \left( 1 + 7.5 \times \frac{f_{Ftuk}}{f_{ctk}} \right) f_{ck} \right]^{1/3} + 0.15 \times \sigma_{cp} \right\} \times b_w \times d \tag{3}$$

8  In equation (3), $\gamma$ is the partial safety factor for concrete, $K$ is a factor related to the size

9  effect that can be calculated according to Eq. (4), $\rho_l$ is the longitudinal reinforcement

10  ratio determined from Eq. (5), $d$ is the effective depth of the cross section and $b_w$ is the

11  width of the web's cross section.

$$K = 1 + \sqrt{\frac{200}{d}} \leq 2.0 \tag{4}$$

$$\rho_1 = \frac{A_{st}}{b_w d} \leq 0.02 \tag{5}$$

12  where $A_{st}$ is the cross sectional area of the longitudinal bars. Also in Eq. (3), $f_{ck}$ is the

13  characteristic value of the FRC compressive strength, while $f_{ctk}$ is its corresponding

14  tensile strength that can be obtained from CEB-FIP 2010 (2011) recommendations:

$$f_{ctk} = 0.3 \left( f_{ck} \right)^{\frac{2}{3}} \tag{6}$$

1    In Eq. (3) $f_{Ftuk}$ is the characteristic value of the ultimate residual flexural tensile strength

2    for FRC that is determined from:

$$f_{Ftuk} = f_{Ftsk} - \frac{w_u}{CMOD_3}\left(f_{Ftsk} - 0.5f_{R,3k} + 0.2f_{R,1k}\right) \tag{7}$$

3    where

$$f_{Ftsk} = 0.45 \times f_{R,1k} \tag{8}$$

4    and

5    $w_u = 1.5$ mm and $CMOD_3 = 2.5$ mm. All the parameters related to the RSFRC can be

6    obtained from the data given in Section 3 and indicated in Table 3.


7    According to RILEM TC 162-TDF, the shear capacity of a SFRC beam is determined

8    from:

$$V_{Rd,3} = V_{cd} + V_{fd} \tag{9}$$

9    where $V_{cd}$ is the concrete contribution determined from Eq. (10)

$$V_{cd} = \left[\left(\frac{0.18}{\gamma}\right) \times K \times \left(100 \times \rho_1 \times f_{fck}\right)^{\left(\frac{1}{3}\right)}\right] \times b_w \times d \tag{10}$$

10   and

$$V_{fd} = 0.7K_f K \tau_{fd} b_w d \tag{11}$$

11   is the contribution of steel fibre reinforcement where:

$$K_f = 1 + n\left(\frac{h_f}{b_w}\right)\left(\frac{h_f}{d}\right) \leq 1.5 \tag{12}$$

$$K = 1 + \sqrt{\frac{200}{d}} \leq 2.0 \tag{13}$$

$$n = \frac{b_f - b_w}{h_f} \leq 3 \tag{14}$$

11

$$\tau_{fd} = \frac{0.18}{\gamma} \times f_{R,4k} \qquad\qquad (15)$$

1   $K_f$ is the factor for taking into account the contribution for the shear resistance of the

2   flange in a T cross section beam, and $\tau_{fd}$ is the design value of the shear strength provided

3   by the fibre reinforcement. In Eq. (12), $h_f$ is the height of the flanges and in Eq. (14), $b_f$

4   is the width of the flanges.


5   *4.2   Experimental program*

6   Figure 13 shows the geometry and reinforcement details of the beams produced for this

7   experimental program, as well as the loading and supporting conditions. Two specimens

8   were tested per each series. Table 5 presents the shear capacity of the tested beams

9   predicted by applying the formulation proposed by CEB-FIP 2010 (2011) and RILEM

10  TC 162-TDF, where characteristic values were adopted for the material properties

11  (according to the equations of both formulations), and $\gamma = 1.5$. In Table 5 the label S_Wj

12  was used to differentiate the tested beams, where "j" identifies the web's cross-section

13  thickness (in mm) of the part of the beam without shear reinforcement.

14      Based on these predictions of the shear capacity, the RSFRC beams were

15  flexurally reinforced with longitudinal steel bars in a percentage assumed sufficient to

16  assure shear failure for all the beams (Figure 13). From tensile tests executed according

17  to EN 10002 (1990) with coupons of the steel stirrups it was obtained an average value

18  (of 4 coupons) of 600.8 MPa and 754.6 MPa for the yield stress and tensile strength,

19  respectively. Four cylinders of 150 mm and 300 mm of height were tested according to

20  NP EN 12390 (2009) and LNEC E397 (1993) for the determination of the average

21  compressive strength (50 MPa) and Young's Modulus (28 GPa), respectively. The Figure

22  14 shows the test setup and position of the five Linear Voltage Displacement Transducers

1    (LVDTs). The effective depth of the cross section ($d$) is 270 mm and the shear span ratio

2    ($a/d$) is 2.65 in order to promote the occurrence of shear failure.

3          The relationship between the applied load and the deflection at the loaded section

4    (LVDT4) of the tested series of beams is represented in Figure 15. By increasing the beam

5    web thickness the load carrying capacity has increased without affecting significantly the

6    deflection at maximum load. In figure 21 the inversion of deflection in the last stage of

7    the loading process of S_W110 and S_W70 beams was caused by the movement of the

8    failure mechanism (Figure 23) formed at this stage in these beams  and the position of the

9    aluminium plate where it touches the piston of the LVDT3 (Figure 14). In fact, at the last

10   stage of the loading process of these beams an upward relieve of deflection was

11   experienced by the top-left part of the beam, where the aforementioned aluminium plate

12   is bonded, leading to the registered inversion of deflection, which will be confirmed by

13   the numerical simulations presented in next section. Table 5 includes the shear capacity

14   of the tested beams, as well as the values predicted according to the RILEM TC 162-TDF

15   and CEB-FIP 2010 (2011) formulations. The ratio between the shear capacity obtained

16   experimentally ($V_{exp}$) and according to the analytical formulations ($V_{ana}$) has decreased

17   with the increase of the beam web thickness. Since design values are being used for the

18   properties of the intervening materials, the $V_{exp}/V_{Rd,ana}$ should be higher than 1.5 in order

19   to guarantee safety predictions for the analytical approach. However, the decrease of the

20   $V_{exp}/V_{Rd,ana}$ with the increase of the width of the web's beam cross section ($b_w$) indicates

21   that the formulations do not consider properly the favourable effect of the fibre orientation

22   when $b_w$ decreases. In fact, fibres become more preferentially aligned with the axis of the

23   beam when $b_w$ decreases due to a more pronounced wall effect, leading to more effective

24   fibre reinforcement mechanisms in terms of arresting the crack propagation (Barros,

1   2011). The irregular shape of the RSF indicates that a higher tendency for this effect is

2   expected when using ISF, due to the higher aspect ratio of these last fibres.


3   *4.3   Numerical simulations*

4   Previous research (Pereira et al., 2008) has indicated that fracture mode I propagation of

5   FRC can be simulated by the trilinear softening diagram represented in Figure 16, whose

6   parameters (fracture energy, $G_f^I$, and values of $\varepsilon_{n,i}^{cr}$ and $\sigma_{n,i}^{cr}$ that define the shape of the

7   diagram that simulates the fracture mode I crack propagation) can be obtained performing

8   inverse analysis with the force-CMOD data (or force-vertical deflection data) registered

9   in three-point notched beam bending tests. In Figure 16, $G_f^I / l_b$ corresponds to the area

10   defined by the trilinear stress-strain normal to the crack plane ($\sigma_n^{cr}$ - $\varepsilon_n^{cr}$), where $l_\text{b}$ is the

11   crack band width. When using a smeared crack approach, the $l_b$ parameter is used in

12   order to assure that the results of the numerical simulations are not dependent of the finite

13   element mesh refinement (Pereira *et al.*, 2008). For this purpose, the $l_b$ is assumed

14   dependent of a geometric characteristic of the finite elements adopted in the numerical

15   simulations. In the present case the $l_b$ was considered equal to the square root of the area

16   of the integration point corresponding to the integration scheme adopted for the

17   evaluation of the stiffness matrix and stress field.

18   The ultimate crack strain, $\varepsilon_{n,u}^{cr}$, is defined as a function of the $\alpha_i$ and $\xi_i$ parameters,

19   fracture energy, $G_f^I$, tensile strength, $f_{ct} = \sigma_{n,1}^{cr}$, and crack band width, $l_b$, as follows (Sena-

20   Cruz 2004),

$$\varepsilon_{n,u}^{cr} = \frac{2}{\xi_1 + \alpha_1 \xi_2 - \alpha_2 \xi_1 + \alpha_2} \frac{G_f^I}{f_{ct} l_b} \tag{16}$$

21   being $\alpha_1 = \sigma_{n,2}^{cr} / \sigma_{n,1}^{cr}$, $\alpha_2 = \sigma_{n,3}^{cr} / \sigma_{n,1}^{cr}$, $\xi_1 = \varepsilon_{n,2}^{cr} / \varepsilon_{n,u}^{cr}$ and $\xi_2 = \varepsilon_{n,3}^{cr} / \varepsilon_{n,u}^{cr}$.

14

1    The objective of the analysis is to evaluate the values of $\alpha_i$, $\xi_i$, and $G_f^I$ of the $\sigma_n^{cr} - \varepsilon_n^{cr}$

2    diagram based on the minimization of the error parameter

$$err = \frac{\left| A_{F-CMOD}^{\exp} - A_{F-CMOD}^{num} \right|}{A_{F-CMOD}^{\exp}} \tag{17}$$

3    where $A_{F-CMOD}^{\exp}$ and $A_{F-CMOD}^{num}$ are the areas below the experimental and the numerical

4    $F-CMOD$ curves, respectively (Barros et al., 2004).

5    In this context, the specimen was modelled with a mesh of 8 node serendipity plane stress

6    finite elements. The Gauss-Legendre integration scheme with 2×2 integration points was

7    used in all elements, with the exception of the elements at the specimen symmetry axis,

8    where 1×2 integration points were used in order to assure that the crack progresses along

9    the symmetry axis of the specimen. In the inverse analysis, the $l_b$ was considered equal to

10   the width of the notch (5 mm) that coincides with the width of the finite elements above

11   the notch. Figure 17 shows the finite element mesh used in the inverse analysis (Sena-

12   Cruz et al., 2004). An average value of $E_c = 28$ GPa was considered for the concrete

13   Young's Modulus. The numerical simulations were carried out with the FEM software

14   FEMIX V4.0 (Sena-Cruz, 2004).

15   The comparison between the average experimental load vs CMOD and numerical

16   load vs CMOD of all tested specimens is shown in Figure 18. The values defining the

17   $\sigma_n^{cr} - \varepsilon_n^{cr}$ diagram obtained from inverse analysis are presented in Table 6, and the

18   graphical representation of these values is presented in Figure 19, where it is visible that

19   the post-cracking residual strength has increased with the content of RSF.

20   A finite element mesh of 144 plane stress elements of 8 nodes was used for the simulation

21   of the beams failing in shear. A Gauss-Legendre integration scheme with 2×2 Integration

22   Points (IP) was used in all the concrete elements. The steel bars were simulated by

1    perfectly bonded 82 elements of two nodes with 2 IP. In the numerical simulation of the

2    beams the incremental approach for the crack shear stress-strain component was used,

3    and the values of the fracture mode I parameters of the smeared crack constitutive model

4    used in the simulations were the same derived from the inverse analysis (see Table 6). In

5    the incremental approach, the two stress components at each crack (crack normal stress,

6    $\sigma_n^{cr}$, and crack shear stress, $\tau_{nt}^{cr}$) are directly determined from their corresponding stress

7    increments, $\Delta\sigma_n^{cr}$ and $\Delta\tau_{nt}^{cr}$. To simulate accurately the deformational response and the

8    crack pattern up to the failure of structures that fail by the formation of a critical shear

9    crack, such as the case of the tested beams, the softening crack shear stress *vs.* crack shear

10    strain relationship, represented in Figure 20, was adopted in the present work. The crack

11    shear stress increases linearly until the crack shear strength is reached, $\tau_{t,p}^{cr}$, (first branch

12    of the shear crack diagram), followed by a decrease in the shear residual strength

13    (softening branch). The diagram represented in Figure 20 is defined by the following

14    equations:

$$\tau_t^{cr}\left(\gamma_t^{cr}\right) = \begin{cases} D_{t,1}\,\gamma_t^{cr} & 0 < \gamma_t^{cr} \le \gamma_{t,p}^{cr} \\ \tau_{t,p}^{cr} - \dfrac{\tau_{t,p}^{cr}}{\left(\gamma_{t,u}^{cr} - \gamma_{t,p}^{cr}\right)}\left(\gamma_t^{cr} - \gamma_{t,p}^{cr}\right) & \gamma_{t,p}^{cr} < \gamma_t^{cr} \le \gamma_{t,u}^{cr} \\ 0 & \gamma_t^{cr} > \gamma_{t,u}^{cr} \end{cases} \tag{18}$$

15    The initial shear fracture modulus, $D_{t,1}^{cr}$, is defined from equation:

$$D_{t,1}^{cr} = \frac{\beta}{1-\beta} G_c \tag{19}$$

16    where $G_c$ is the elastic shear modulus of RSFRC and $\beta$ is the shear retention factor that

17    should be in the range ]0,1[. The peak crack shear strain, $\gamma_{t,p}^{cr}$, is obtained using the crack

18    shear strength (from the input data), $\tau_{t,p}^{cr}$, and the crack shear modulus:

$$\gamma_{t,p}^{cr} = \frac{\tau_{t,p}^{cr}}{D_{t,1}^{cr}} \qquad (20)$$

1    The ultimate crack shear strain, $\gamma_{t,u}^{cr}$, depends on the crack shear strength, $\tau_{t,p}^{cr}$, on the

2    shear fracture energy (mode II fracture energy), $G_{f,s}$, and on the crack band width, $l_b$:

$$\gamma_{t,u}^{cr} = \frac{2G_{f,s}}{\tau_{t,p}^{cr} \, l_b} \qquad (21)$$

3    In the present approach it is assumed that the crack band width is the same for both

4    fracture mode I and mode II processes, but specific research should be done in this respect

5    in order to assess the influence of these model parameters on the predictive performance

6    of the behaviour of elements failing in shear. Five shear crack statuses are proposed and

7    their meaning is schematically represented in Figure 20.

8    The crack mode II modulus of the first linear branch of the diagram is defined by equation

9    (19), while the second linear softening branch is defined by

$$D_{t,2}^{cr} = -\frac{\tau_{t,p}^{cr}}{\gamma_{t,u}^{cr} - \gamma_{t,p}^{cr}} \qquad (22)$$

10    and the crack shear modulus of the unloading and reloading branches is obtained from

$$D_{t,3-4}^{cr} = \frac{\tau_{t,\max}^{cr}}{\gamma_{t,\max}^{cr}} \qquad (23)$$

11    being $\gamma_{t,\max}^{cr}$ and $\tau_{t,\max}^{cr}$ the maximum crack shear strain already attained and the

12    corresponding crack shear stress determined from the softening linear branch. Both

13    components are stored to define the unloading/reloading branch (see Figure 20).

14    In free-sliding status ($|\gamma_t^{cr}| > |\gamma_{t,u}^{cr}|$) the crack shear modulus, $D_{t,5}^{cr}$, is null. To avoid

15    numerical instabilities in the calculation of the stiffness matrix and in the calculation of

16    the internal forces, when the crack shear status is free-sliding, a residual value is assigned

17    to this term. A free-sliding status is assigned to the shear crack when $\varepsilon_n^{cr} > \varepsilon_{n,u}^{cr}$. The details

1    about how the shear crack statuses were treated can be consulted elsewhere (Ventura-

2    Gouveia, 2011).

3       Table 7 includes the values of the model parameters adopted in the numerical

4    simulations of the tested beams. For the concrete Young's modulus a small reduction was

5    made following the recommendations of CEB-FIP Model Code for material nonlinear

6    analysis (90% was assumed). To take into account the residual tensile stresses due to

7    shrinkage, the in-situ tensile strength of the concrete, $f_{ct}$, is taken as $0.3\sqrt{f_{cm}} = 1.9$ MPa.

8    To simulate the behaviour of the longitudinal and transversal steel bars a linear stress-

9    strain diagram with an elasticity modulus of 200 GPa was assumed, since preliminary

10   numerical analysis have indicated a maximum strain of 1.9‰, which is less than the yield

11   strain of these reinforcements.

12      The experimental and the numerical relationships between the applied load and

13   the deflection at the mid-span section for the tested beams are compared in Figure 21, and

14   the comparison of the shear capacity of the RC beams registered experimentally and

15   obtained from numerical simulations is depicted in Figure 22. The model has captured

16   with high accuracy the deformational response of the tested beams, even the inversion of

17   deflection when the failure mechanism occurred in the S_W70 and S_W110 beams. This

18   effect was not occurred in the S_W150 beam since the T cross shape of the other beams

19   favour the occurrence of the aforementioned movement of the failure mechanism. The

20   maximum average strain in the longitudinal steel bars of the S_W150 was 1.9‰, which

21   indicates that these RSF have potential to convert a brittle shear failure mode in a ductile

22   flexural failure mode for these type of structural elements if a higher post-cracking

23   residual strength is assured for the RSFRC.

24      To assess the effectiveness of the RSF in terms of shear reinforcement, the

25   previous numerical model was used for simulating the same series of beams but for the

18

1   following content of fibres: 0 (plain concrete, PC, of the same strength class of RSFRC);

2   45 kg/m$^3$ and 90 kg/m$^3$. The model parameters are those indicated in Table 7. For the

3   fracture mode I of RSFRC beams they correspond to the values obtained from inverse

4   analysis that are indicated in Table 6, while for the plain concrete beams they were

5   obtained according to the recommendation of CEB-FIP 2010( 2011). From these

6   simulations the results presented in Table 8 were obtained, showing that the RSF shear

7   reinforcement efficiency increases with the decrease of the thickness of the web's cross

8   section, and, as expected, with the content of RSF. For the S_W70 a maximum increase

9   of 95% was obtained when using 90 kg/m$^3$ of RSF.

10  **5  Conclusions**

11  The first part of this work was dedicated to evaluate the mechanical properties of

12  Recycled Steel Fibre Reinforced Concrete (RSFRC), and to the comparison to those

13  determined from Industrial Steel Fibre Reinforced Concrete (ISFRC). The properties

14  were obtained by executing three point notched beam bending tests. The second part of

15  the paper was dedicated to the assessment of the benefits of RSF for the shear

16  reinforcement of shallow RC beams failing in shear. On the basis of the results presented

17  in this work, the following concluding remarks can be highlighted:

18      1) From the three point notched beam bending tests results it was verified that the

19          deflection hardening phase registered in the ISFRC specimens was not developed

20          in the RSFRC specimens. This indicates that the fibre reinforcement mechanisms

21          for relatively small crack width levels were not as effective in the RSF as were in

22          the ISF, due to the geometry and surface characteristics of RSF fibres. However,

23          the flexural strength of RSFRC specimens was almost constant and of the same

19

1　　　　order of the flexural tensile strength up to the ultimate crack width recorded in the

2　　　　executed tests.

3　　2) An almost linear relationship between $f_{eq,2}$ and $f_{eq,3}$ was obtained, which was a

4　　　　trend already observed in ISFRC. The same tendency was also observed between

5　　　　the concept of residual flexural strength and equivalent flexural strength ( $f_{eq,2}$ vs

6　　　　$f_{R,1}$ and $f_{eq,3}$ vs $f_{R,4}$ ), which was also already been registered in ISFRC.

7　　3)　From a database containing the results of the characterization of the post-cracking

8　　　　behaviour of ISFRC it was verified that RSFRC results have a similar trend of the

9　　　　corresponding results of the ISFRC of this database ( $f_{R,1} - f_{R,3}$ and $f_{R,1} - f_{R,4}$ ).

10　　　　However, the residual flexural strengthening parameters ( $f_{R,i}$ ) of ISFRC have

11　　　　increased more pronouncedly with the fibre volume percentage ($V_f$) than in the

12　　　　case of RSFRC, which means that for a certain post-cracking performance a

13　　　　higher $V_f$ of RSF is necessary. However, the $f_{R,i}$ values obtained for the

14　　　　developed RSFRC are sufficiently high to create good perspectives for the use of

15　　　　this reinforcement in certain applications, such are the cases of concrete block

16　　　　foundations, slabs supported on soil or on piles.

17　On the basis of the results of the tests with RSFRC beams failing in shear, it was observed

18　that the ratio of the shear capacity obtained experimentally to that calculated using

19　RILEM and *fib* guidelines has decreased with the increase of the beam web thickness,

20　which indicates that both formulations require some enhancements for better consider the

21　geometry of the beam in order to more accurately simulate the fibre orientation and

22　distribution on the effectiveness of the fibre reinforcement mechanisms.

The tests with RSFRC beams failing in shear were numerically simulated by performing material nonlinear analysis with a smeared crack model under the framework of the finite element method, where the fracture mode I parameters of the crack constitutive model was determined by executing inverse analysis with the force-CMOD data registered in three-point notched beam bending tests. The good predictions in terms of load carrying and deflection capacity evidenced that this numerical strategy is suitable to predict the behaviour of RSFRC beams failing in shear. By using this model and adopting a plain concrete of the same strength class of the RSFRC used in the tested RC beams, it was verified that 90 Kg/m$^3$ of RSF provided an increase of 95%, 81% and 71% in terms of shear capacity of the beams with a web's thickness of 70, 110 and 150 mm, respectively, when the shear capacity of the reference beam (plain concrete with the same flexural reinforcing ratio) is considered for comparison purpose." For a more comprehensive assessment of the shear reinforcement effectiveness of RSF, real scale beams should be tested in order to avoid a detrimental impact of the scale effect on the results.

# 7 References

ACI Committee 318, (2008). Building code requirements for structural concrete and commentary. appendix A, strut-and-tie models ed. s.l.:American Concrete Institut.

Aiello, M. A., Leuzzi, F., Centonze, G. & Maffezzoli, A., (2009). "*Use of steel fibres recovered from waste tyres as reinforcement in concrete: Pull-out behaviour, compressive and flexural strength.*" Waste Management, 29(6), pp. 1960-1970.

AMAT, 2003. "*Advanced molecular agitation technology*" from www.amat-ltd.com. [Online].

Amin, A., Foster, S. J. & Muttoni, A., (2013). "*Evaluation of the tensile strength of SFRC as derived from inverse analysis of notched bending tests.*" Toledo, FraMCoS-8.

Aoude, A. F., Belghiti, M., cook, W. D. & Mitchell, D., (2012). "*Response of steel fibre-reinforced concrete beams with and without stirrups.*" ACI Structure Journal, 109(3), pp. 359-368.

Banthia, N., Krstulovic, N. & Galiant, M., (2010). "*Report on the Physical Properties and Durability of Fiber-Reinforced Concrete.*" ACI 544.5R-10, Reported by ACI Committee 544.

Barros, J. A., Lourenço, L. A., Soltanzadeh, F. & Taheri, M., (2014). "*Steel fibre reinforced concrete for elements failing in bending and in shear*." European Journal of Environmental and Civil Engineering, 18(1), pp. 33-65.

Barros, J.A.O., "*Technology, design and applications of steel fibre reinforced self compacting concrete*", 6th International Conference Fibre Concrete 2011 Technology, Design, Application, CTU in Prague, Masarykova kolej, 8 and 9 September 2011. (Invited Keynote Lecturer)

Barros, J. A., di Prisco, M. & di Prisco, C., (2009). "*Modelling FRC infrastructures taking into account the soil-structure interaction*" Barcelona.

Barros, J. A., Cunha, V. M., Ribeiro, A. F. & Antunes, J. A., (2005). "*Post-cracking behaviour of steel fibre reinforced concrete*" Materials and Structures, 31(1), pp. 47-56.

Barros, J.A.O., Gettu, R. and Barragan, B.E., (2004). "*Material nonlinear analysis of steel fibre reinforcedconcrete beams failing in shear*", Proceeding of 6th

International RILEM Symposium on fibre reinforced concrete - BEFIB 2004, Edts. M. di Prisco, R. Felicetti, G.A. Plizarri, 1, pp. 711-720.

Barros, J. A. & Figueiras, J., (1999). "*Flexural Behaviour of SFRC: Testing and Modeling.*". Materials in civil engineering, 11(4), pp. 331-339.

fib Model Code 2010, CEB and FIP, 2011.

Caggiano, A., Cremona, M., Faella, C., Lima, C. & Martinelli, E. (2012). "Fracture behavior of concrete beams reinforced with mixed long/short steel fibers" Construction and Building Materials, 37, pp. 832-840

Centonze, G., Leonard, M. & Aiello, M. A., (2012). "*Steel fibres from waste tyres as reinforcement in concrete: A mechanical characterization.*" Construction and Building Materials, Volume 36, pp. 46-57.

Cucchiara, C., Mendola, L. L. & Papia, M., (2004). "*Effectiveness of stirrups and steel fibres as shear reinforcement.*" Cement & Concrete Composites, 26(7), pp. 777-786.

Cunha, V., (2010). "*Steel Fibre Reinforced Self-Compacting Concrete (from Micro-Mechanics to Composite Behaviour)*" PhD Thesis, University of Minho.

De Montaignac, R., Massicotte, B. & Charron, J. P., (2012). "*Design of Sfrc Structural Elements: Flexural Behaviour Prediction.*" Materials and Structures, 45(4), pp. 623-636.

EN 10 002-1:1990. Metallic materials - Tensile testing. Part 1: Method of test (at ambient temperature). CEN, Brussels, Belgium, 35 pp.

Eurocode 2, (2004). Design of concrete structures - Part 1-1: General rules and rules for buildings. Brussels: Comité Européen de Normalisation (CEN), EN 1992-1-1:2004.

Graeff, A., Pilakoutas, K., Neocleous, K. & Peres, M. V., (2012). "*Fatigue resistance and cracking mechanism of concrete pavements reinforced with recycled steel fibres recovered from post-consumer tyres.*" Engineering Structure, Volume 45, pp. 385–395.

Granju, J. & Balouch, S., (2005). "*Corrosion of steel fibre reinforced concrete from the cracks.*" Cement and Concrete Research, 35(3), pp. 572-577.

Hai, H., (2009). "*Shear Behaviour Of Steel Fibre Reinforced Concrete Beams Withou Stirrup Reinforcement.*" A dissertation submitted in partial fulfillment of the requirements of the degree of Ph.D, University of Michigan.

Kunieda, M., Ueda, N. & Nakamura, H. (2014). "Ability of recycling on fiber reinforced concrete." Construction and building materials, 67, pp. 315-320.

Lee, S., Cho, J. & Vecchio, F. J., (2011). "*Diverse Embedment Model for Fibre-Reinforced Concrete in Tension: Model Development.*" ACI Materials Journal, 108(5), pp. 516-525.

LNEC E397-1993:1993. Concrete – Determination of the elasticity young modulus under compression. Portuguese specification from LNEC.

Lourenço, L., Barros, J. A., Alves, J., (2011). "*Fiber reinforced concrete of enhanced fire resistance for tunnel segments.*" ACI SP-276-4, Durability enhancements in concrete with fiber reinforcement, Editors: Corina-Maria Aldea and Nur Yazdani, March.

Meda, A., Minelli, F., Plizzari, G. A. & Riva, P., (2005). "*Shear behaviour of steel fibre reinforced concrete beams.*" Materials and Structures, 38(3), pp. 343-353.

Moraes Neto, B. N., (2013). "*Punching behaviour of steel fibre reinforced concrete slabs submitted to symmetric loading.*" PhD in Civil Engineering, Department of Civil and Environmental Engineering, University of Brasília, Brasília, DF,.

Neocleous, K., Tlemat, H. & Pilakoutas, K., (2006). "*Design Issues for Concrete Reinforced with Steel Fibres, Including Fibres Recovered from Used Tyres.*" Materials in Civil engineering, 18(5), pp. 677–685.

NP EN 12390-3:2009. Testing hardened concrete. Part 3: Compressive strength of test specimens.

NZS4203, (1992). General structural design and design loadings for buildings, standard published 12/14/1992 by Standards New Zealand.

Pereira, E. B., Barros, J. A. & Camões, A. F., (2008). "*Steel fibre reinforced self-compacting concrete–experimental research and numerical simulation.*" Structural engineering, 134(8), pp. 1310-1321.

RILEM TC 162-TDF, (2003). "*Test and design methods for steel fibre reinforced concrete: σ -ε design method - Final Recommendation.*" Materials and Structures, Volume 36, pp. 560-567.

Safeer, H., Ahmed, M. & Moncef, L., (2004). "*Experimental study on settlement and punching behaviour of full-scale RC and SFRC precast tunnel lining segments.*" Engineering Structures, 72(1), pp. 1-10.

Sena-Cruz, J.M. (2004). *"Strengthening of concrete structures with near-surface mounted CFRP laminate strips"*, PhD Thesis, Department of Civil Engineering, University of Minho, http://www.civil.uminho.pt/composites.

Sena-Cruz, J. M. et al., (2004). *"Stress crack opening relationship of enhanced performance concrete."* 9th Portuguese Conference on Fracture, ESTSetúbal, Portugal,. s.l., s.n., pp. 395-403.

Susetyo, J., Gauvreau, P. & Vecchio, F. J., (2011). *"Effectiveness of Steel Fibre as Minimum Shear Reinforcement."* ACI Structural Journal, 108(4), pp. 488-496.

Tlemat, H., Pilakoutas, K. & Neocleous, K., (2006). *"Modelling of SFRC using inverse finite element analysis."* Materials and Structures, 93(2), pp. 221-233.

Tlemat, H., Pilakoutas, K. & Neocleous, K., (2004). *"Demonstrating steel fibres from waste tyres as reinforcement in concrete."* Material characterisation, Proceedings of the First International Conference on Innovative Materials and Technologies for Construction and Restoration.

Ventura-Gouveia, A., (2011). *"Constitutive models for the material nonlinear analysis of concrete structures including time dependent effects"*. PhD Thesis, Department of Civil Engineering, University of Minho.

Ventura-Gouveia, A., Barros, J. A. & Azevedo, A. F., (2011). *"Crack constitutive model for the prediction of punching failure modes of fibre reinforced concrete laminar structures."* Computers and Concrete, 8(6), pp. 735-755.

Voo, J. Y. & Foster, S. J., (2003). *"Variable Engagement Model for Fibre Reinforced Concrete in Tension."* Sydney, Australia: The University of New South Wales.

## 8    Table captions

Table 1- Designation of the series of tests of the experimental program
Table 2 - Mix proportions [Kg per cubic meter of concrete]
Table 3 - Equivalent and residual flexural tensile strength parameters for RSFRC [MPa]
Table 4 - Equivalent and residual flexural tensile strength parameters for ISFRC [MPa]
Table 5 - Shear capacity according to analytical formulations and experimental tests
Table 6 - Values defining the tensile softening diagram, obtained from inverse analysis
Table 7- Values of the model parameters in the numerical simulations of the tested RC
beams
Table 8- Increase of shear capacity provided by RSF

Table 1- Designation of the series of tests of the experimental program

| Mix | Type of fibres | Series name | Number of specimens | Content of steel fibers [kg / m³] |
|---|---|---|---|---|
| MRSF_45 | RSF | RSFRC45 | 10 | 45 |
| MRSF_60 | RSF | RSFRC60 | 10 | 60 |
| MRSF_90 | RSF | RSFRC90 | 4 | 90 |
| MISF_45 | ISF | ISFRC45 | 4 | 45 |
| MISF_60 | ISF | ISFRC60 | 4 | 60 |
| MISF_90 | ISF | ISFRC90 | 4 | 90 |

Table 2 - Mix proportions [Kg per cubic meter of concrete]

| Mix | C | LF | W | SP | FRS | CRS | CA | FA | SF |
|-----|-----|-----|-----|-----|-----|-----|-----|-----|-----|
| **M_45** | 380.5 | 326.2 | 126.8 | 6.09 | 362.6 | 574.6 | 510.1 | - | 45 |
| **M_60** | 380.5 | 353.0 | 140.0 | 7.83 | 237.0 | 710.0 | 590.0 | - | 60 |
| **M_90** | 408.0 | 395.0 | 150.0 | 6.26 | 263.0 | 658.0 | 446.0 | 73.0 | 90 |

C = Cement; LF = Limestone Filler; W = Water; SP = Superplasticizer; FRS = Fine River Sand; CRS = Coarse River Sand; CA = Crushed Aggregates; FA = Fly Ash; SF = Steel fibres (ISF or RSF)

Table 3 - Equivalent and residual flexural tensile strength parameters for RSFRC [MPa]

| Series | | $f_{fct,L}$ | $f_{eq,2}$ | $f_{eq,3}$ | $f_{R,1}$ | $f_{R,2}$ | $f_{R,3}$ | $f_{R,4}$ |
|---|---|---|---|---|---|---|---|---|
| RSFRC45 | Average | 4.73 | 4.28 | 3.90 | 4.16 | 3.94 | 3.69 | 3.43 |
| | COV | 18.6% | 28.9% | 30.8% | 24.6% | 32.4% | 33.4% | 33.5% |
| RSFRC60 | Average | 5.00 | 5.39 | 5.08 | 5.36 | 5.17 | 4.86 | 4.41 |
| | COV | 11.4% | 15.2% | 16.8% | 13.6% | 17.2% | 18.6% | 20.7% |
| RSFRC90 | Average | 4.56 | 6.78 | 6.35 | 6.62 | 6.56 | 5.90 | 5.55 |
| | COV | 9.5% | 8.3% | 9.3% | 7.6% | 9.1% | 11.9% | 12.2% |

Table 4 - Equivalent and residual flexural tensile strength parameters for ISFRC [MPa]

| Series | | $f_{fct,L}$ | $f_{eq,2}$ | $f_{eq,3}$ | $f_{R,1}$ | $f_{R,2}$ | $f_{R,3}$ | $f_{R,4}$ |
|---|---|---|---|---|---|---|---|---|
| ISFRC45 | Average | 5.14 | 8.66 | 7.87 | 8.61 | 8.36 | 6.83 | 5.64 |
| | COV | 4.9% | 25.5% | 24.3% | 25.0% | 23.0% | 24.3% | 21.9% |
| ISFRC60 | Average | 6.62 | 10.49 | 7.24 | 10.43 | 7.39 | 4.86 | 3.40 |
| | COV | 6.7% | 12.8% | 13.0% | 13.3% | 19.1% | 21.7% | 20.4% |
| ISFRC90 | Average | 5.99 | 12.75 | 11.31 | 12.37 | 12.00 | 9.71 | 7.38 |
| | COV | 10.5% | 12.1% | 22.7% | 11.9% | 25.3% | 34.2% | 37.2% |

Table 5 - Shear capacity according to analytical formulations and experimental tests

| Specimen | $V_{\text{exp}}$ [kN] | $V_{\text{Rd,RILEM}}$ [kN] | $V_{\text{exp}}/V_{\text{Rd,RILEM}}$ | $V_{\text{Rd,FIB}}$ [kN] | $V_{exp}/V_{\text{Rd,FIB}}$ |
|---|---|---|---|---|---|
| S_W70 | 81.290 | 29.806 | 2.72 | 26.042 | 3.121 |
| S_W110 | 95.810 | 45.356 | 2.11 | 41.690 | 2.298 |
| S_W150 | 109.172 | 56.497 | 1.93 | 51.266 | 2.129 |

Table 6 - Values defining the tensile softening diagram, obtained from inverse analysis

| Series | $\sigma_{n,1}^{cr}$ [N / mm²] | $\xi_1$ | $\alpha_1$ | $\xi_2$ | $\alpha_2$ | $G_f^I$ [N / mm] |
|--------|------|-------|-------|-------|-------|-------|
| RSFRC45 | 2.250 | 0.012 | 0.650 | 0.280 | 0.520 | 6.000 |
| RSFRC60 | 2.300 | 0.032 | 0.750 | 0.350 | 0.730 | 6.300 |
| RSFRC90 | 2.620 | 0.100 | 0.930 | 0.600 | 0.730 | 7.700 |

Table 7- Values of the model parameters in the numerical simulations of the tested RC beams

| Property | Value |
|---|---|
| Poisson's ratio ($\nu_c$) | 0.20 |
| Initial Young's Strength ($E_c$) | 25000 N/mm² |
| Compressive strength ($f_c$) | 40 N/mm² |
| Trilinear tension-softening diagram | $f_{ct}$=1.9 N/mm²<br><br>For RSFRC: $\alpha_i$, $\xi_i$, and $G_f^I$ in Table 6<br><br>For PC: $\alpha_1$ =0.20, $\alpha_2$ =0.26, $\xi_1$ =0.20, $\xi_2$ =0.18; $G_f^I$ =0.148 |
| Crack shear stress-crack shear strain softening diagram | For PC: $\beta$ =0.1, $\tau_{t,p}^{cr}$ =1.5 MPa, $G_{f,s}$ =3.0 N/mm<br><br>For RSFRC of 45 kg/m³: $\beta$ =0.1, $\tau_{t,p}^{cr}$ =1.5 MPa, $G_{f,s}$ =3.0 N/mm<br><br>For RSFRC of 60 kg/m³: $\beta$ =0.1, $\tau_{t,p}^{cr}$ =1.5 MPa, $G_{f,s}$ =3.0 N/mm<br><br>For RSFRC of 90 kg/m³: $\beta$ =0.1, $\tau_{t,p}^{cr}$ =1.5 MPa, $G_{f,s}$ =3.0 N/mm |
| Crack band width, $l_b$ | Square root of the area of Gauss integration point |
| Threshold angle (Sena-Cruz, 2004) | $\alpha_{th}$=30° |
| Maximum number of cracks per integration point (Sena-Cruz, 2004) | 2 |

Table 8- Increase of shear capacity provided by RSF

| Specimen | RSFRC45 | RSFRC60 | RSFRC90 |
|----------|---------|---------|---------|
| S_W70 | 74% | 82% | 95% |
| S_W110 | 67% | 74% | 81% |
| S_W150 | 59% | 66% | 71% |

## 9 Figure captions

Figure 1. Overview of the industrial process to transform tires in fibres for use in the reinforcement of concrete: a) waste tires to be recycled, b) waste tires transformed in pieces of rubber, c) stock of pieces of rubber, d) cryogenic tunnel to put tires in the glassy state, e) tunnel hammers to break the pieces of rubber in glassy state and f) the fibres are separated by magnetic and collected in a container

Figure 2. Recycled steel fibres extracted from wasted tires

Figure 3.Three point beam bending test setup

Figure 4. Typical load F – CMOD curve of FRC (CEB-FIP 2010, 2011)

Figure 5. Flexural behaviour in three point notched beam bending tests: a) RSFRC, b) ISFRC

Figure 6. Comparison of the flexural behaviour of ISFRC and RSFRC

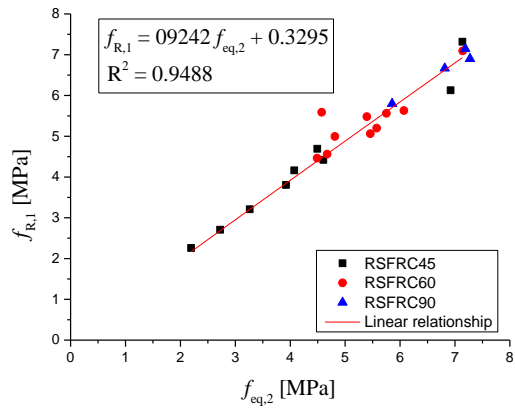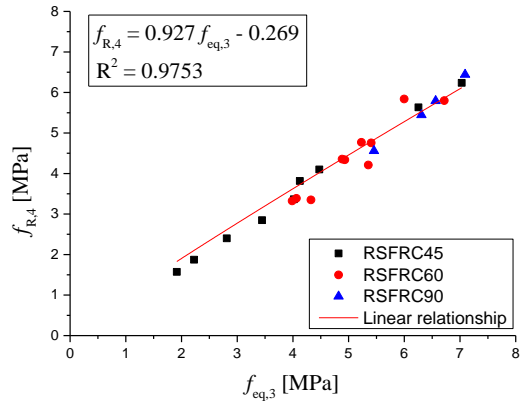Figure 7. Representation of the $f_{eq}$ and $f_{R,i}$ parameters for the series: a) RSFRC, b) ISFRC
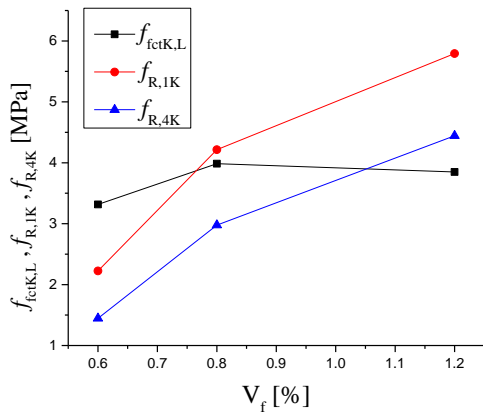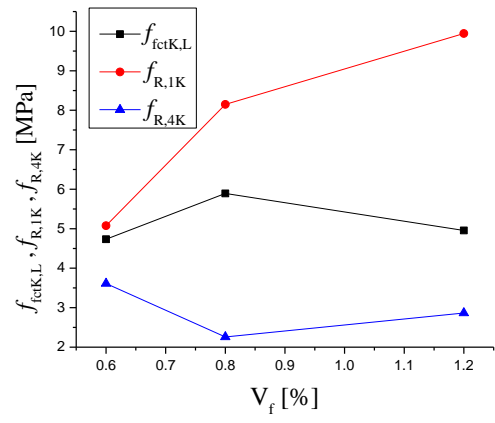
Figure 8. Relationship between $f_{eq,2}$ and $f_{eq,3}$

Figure 9. Relationship between: a) $f_{eq,2}$ and $f_{R,1}$, b) $f_{eq,3}$ and $f_{R,4}$ for RSFRC

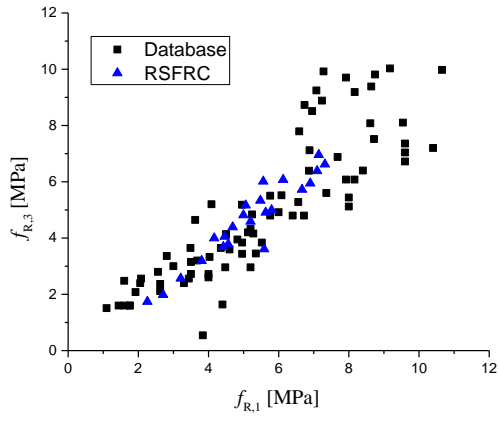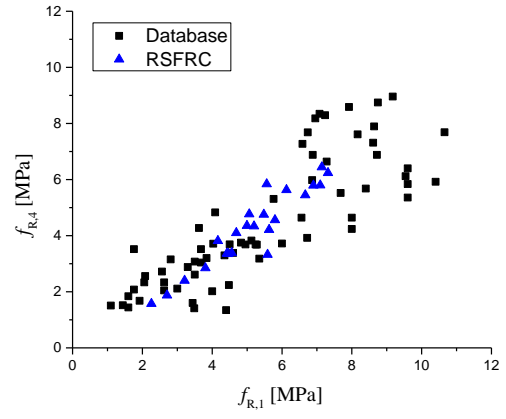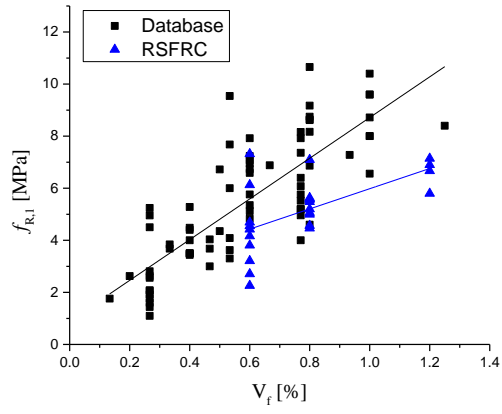Figure 10. Relationship between: $f_{fctk,L}, f_{R,1K}, f_{R,4K}$ and $V_f$ : a) RSFRC and b) ISFRC
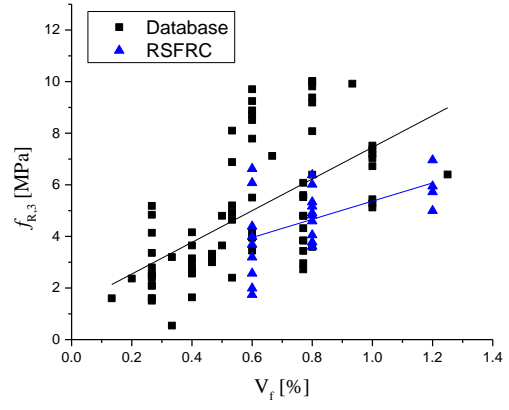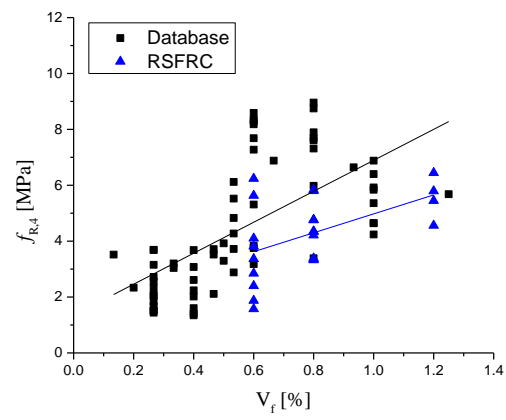
Figure 11. Relationship between: a) $f_{R,1}$ and $f_{R,3}$ and b) $f_{R,1}$ and $f_{R,4}$ (RSFRC and DB)

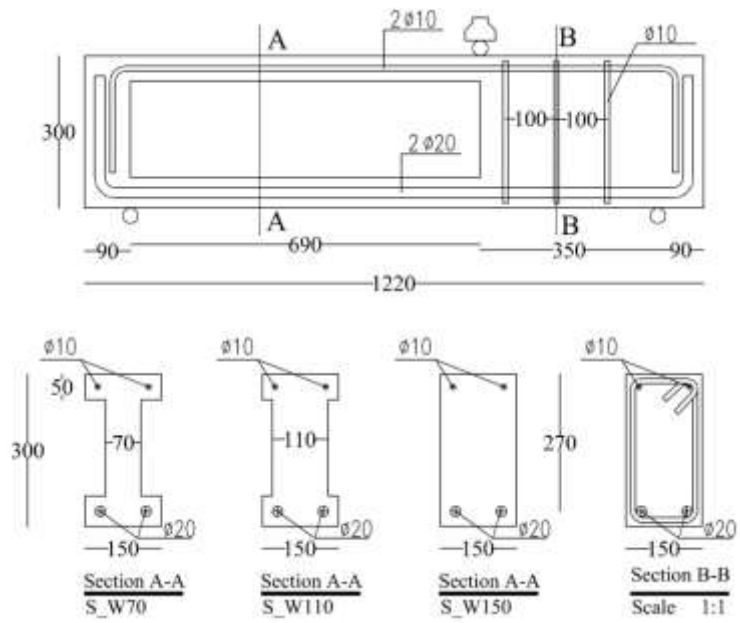Figure 12. Influence of $V_f$ on: a) $f_{R1}$, b) $f_{R3}$, and b) $f_{R,4}$ (RSFRC and DB)

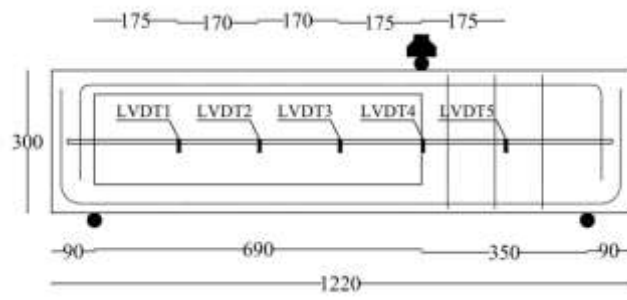Figure 13. Geometry of the beams (dimensions in mm)

Figure 14. Beam configuration, test setup and position of the LVDTs (dimensions in mm)
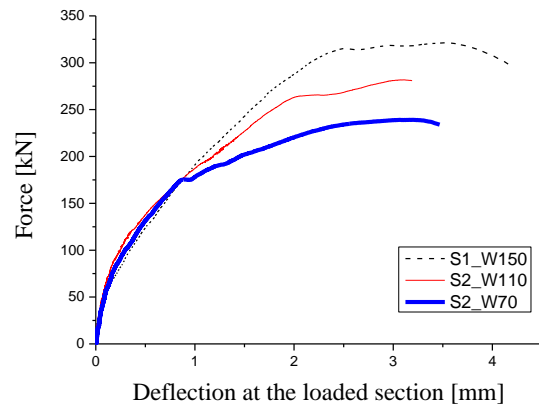
Figure 15. Load - deflection relationship at the loaded section for the tested series of beams

Figure 16. Trilinear stress-strain diagram to simulate the fracture mode I crack propagation ( $\sigma_{n,2}^{cr} = \alpha_1 \; \sigma_{n,1}^{cr}$ , $\sigma_{n,3}^{cr} = \alpha_2 \; \sigma_{n,1}^{cr}$ , $\varepsilon_{n,2}^{cr} = \xi_1 \; \varepsilon_{n,u}^{cr}$ , $\varepsilon_{n,3}^{cr} = \xi_2 \; \varepsilon_{n,u}^{cr}$ ).

Figure 17. Finite element mesh adopted in the inverse analysis

Figure 18. Average experimental load vs deflection and numerical load vs deflection

Figure 19. Tensile softening trilinear diagrams obtained from inverse analysis

Figure 20. Diagram to simulate the relationship between the crack shear stress and crack shear strain component, and possible shear crack statuses

Figure 21. Comparison of the experimental and numerical load-deflection curves of the bending tests with T-shape beams failing in shear: a) S_W150, b) S_W110 and c) S_W70

Figure 22.Comparison of the shear capacity of the RC beams registered experimentally and obtained from numerical simulations

Figure 23. Crack pattern at failure of the beams: a) S_W150, b) S_W110, c) S_W70

Figure 1. Overview of the industrial process to transform tires in fibres for use in the reinforcement of concrete: a) waste tires to be recycled, b) waste tires transformed in pieces of rubber, c) stock of pieces of rubber, d) cryogenic tunnel to put tires in the glassy state, e) tunnel hammers to break the pieces of rubber in glassy state and f) the fibres are separated by magnetic and collected in a container

Figure 2. Recycled steel fibres extracted from wasted tires

Figure 3.Three point beam bending test setup

Figure 4. Typical load F – CMOD curve of FRC (CEB-FIP 2010, 2011)

Figure 5. Flexural behaviour in three point notched beam bending tests: a) RSFRC, b) ISFRC

Figure 6. Comparison of the flexural behaviour of ISFRC and RSFRC

Figure 7. Representation of the $f_{eq}$ and $f_{R,i}$ parameters for the series: a) RSFRC, b) ISFRC

Figure 8. Relationship between $f_{eq,2}$ and $f_{eq,3}$

Figure 9. Relationship between: a) $f_{eq,2}$ and $f_{R,1}$, b) $f_{eq,3}$ and $f_{R,4}$ for RSFRC

Figure 10. Relationship between: $f_{fctk,L}, f_{R,1K}, f_{R,4K}$ and $V_f$ : a) RSFRC and b) ISFRC

Figure 11. Relationship between: a) $f_{R,1}$ and $f_{R,3}$ and b) $f_{R,1}$ and $f_{R,4}$ (RSFRC and DB)

Figure 12. Influence of $V_f$ on: a) $f_{R1}$, b) $f_{R3}$, and b) $f_{R,4}$ (RSFRC and DB)

Figure 13. Geometry of the beams (dimensions in mm)

Figure 14. Beam configuration, test setup and position of the LVDTs (dimensions in mm)

Figure 15. Load - deflection relationship at the loaded section for the tested series of beams

Figure 16. Trilinear stress-strain diagram to simulate the fracture mode I crack propagation ( $\sigma_{n,2}^{cr} = \alpha_1 \sigma_{n,1}^{cr}$ , $\sigma_{n,3}^{cr} = \alpha_2 \sigma_{n,1}^{cr}$ , $\varepsilon_{n,2}^{cr} = \xi_1 \varepsilon_{n,u}^{cr}$ , $\varepsilon_{n,3}^{cr} = \xi_2 \varepsilon_{n,u}^{cr}$ ).

Figure 17. Finite element mesh adopted in the inverse analysis

Figure 18. Average experimental load vs deflection and numerical load vs deflection

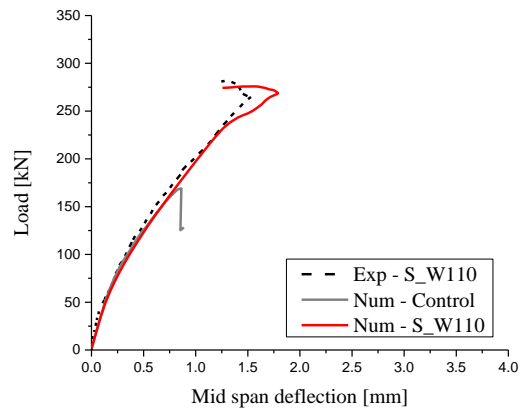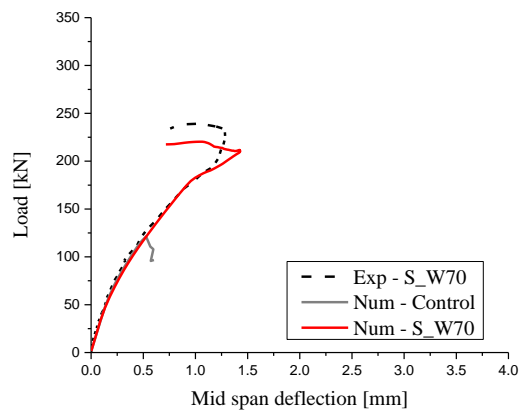Figure 19. Tensile softening trilinear diagrams obtained from inverse analysis

Figure 20. Diagram to simulate the relationship between the crack shear stress and crack shear strain component, and possible shear crack statuses

a)

b)



c)

Figure 21. Comparison of the experimental and numerical load-deflection curves of the bending tests with T-shape beams failing in shear: a) S_W150, b) S_W110 and c) S_W70
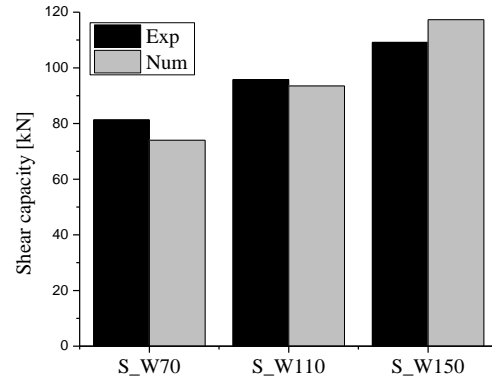
Figure 22.Comparison of the shear capacity of the RC beams registered experimentally and obtained from numerical simulations

a)



b)



c)

Figure 23. Crack pattern at failure of the beams: a) S_W150, b) S_W110, c) S_W70